Spectrum of Engineering Sciences
ISSN (e) 3007-3138 (p) 3007-312X Volume 4, Issue 4, 2026

G-C_3N_4/CEO_2 DEPOSITED WITH PT COCATALYST FOR PHOTOCATALYTIC CO_2 REDUCTION: A COMPREHENSIVE REVIEW

[1]Mahrukh Akram, [2]Dr. Abdul Razaq,[3]Shabir Ahmed Dharejo, [4]Zubair Ahmed Chachar
PhD chemistry Department of chemistry Govt college university Faisalabad
alislahschool372@gmail.com
Ph.D School of Chemistry, University of the Punjab, Lahore-
arazaqch@gmail.com
PhD Scholar Institute of Chemistry Shah Abdul Latif University Khairpur Mir's
shabirdharejo@gmail.com
PhD Chemistry Scholor Institute of Chemistry, Shah Abdul Latif University Khairpur
Zubairahmedchachar@gmail.com*

Keywords- *photocatalysis, CO_2 reduction, g-C_3N_4, CeO_2, platinum cocatalyst, heterojunction, charge separation*

Article History
Received on 01 April, 2026
Accepted on 26 April, 2026
Published on 28 April, 2026

Corresponding Author:

Abstract

The escalating concentration of atmospheric carbon dioxide (CO_2) necessitates innovative mitigation strategies. Photocatalytic CO_2 reduction offers a solar-driven route to convert CO_2 into value-added fuels and chemicals. This review presents a comprehensive investigation of a ternary photocatalytic system comprising graphitic carbon nitride (g-C_3N_4) and cerium dioxide (CeO_2), enhanced by platinum (Pt) as a noble metal cocatalyst. The synergistic interactions between g-C_3N_4 and CeO_2 yield superior charge separation, broadened light absorption, and enhanced surface reactivity. Characterisation by XRD, FTIR, TEM, SEM, and UV-Vis spectroscopy confirmed successful composite synthesis with preserved crystal structures and markedly enlarged BET surface areas (up to 36.65 m^2/g for CeO_2-g-C_3N_4 (3) versus 9.45 m^2/g for pure CeO_2). Stable production of CH_4 (~ 30 μmol/g/h) and H_2 (~ 35 μmol/g/h) was demonstrated over five consecutive photocatalytic cycles. These findings advance understanding of ternary heterojunction photocatalysts for sustainable CO_2 valorisation.

1. Introduction

Atmospheric CO_2 concentrations have risen dramatically since industrialisation, making climate-change mitigation a global priority (Solomon et al., 2009). Photocatalytic CO_2 reduction has emerged as a promising solar-driven strategy that simultaneously reduces atmospheric CO_2 and generates renewable fuels, mimicking natural photosynthesis (Zhu and Wang, 2017). The efficiency of this process depends on three coupled steps: light absorption to generate electron–hole pairs, efficient charge separation, and selective surface catalytic reactions (Saravanan et al., 2021).

Traditional photocatalysts such as TiO_2 are constrained by their wide bandgap (~ 3.2 eV), restricting absorption to ultraviolet light and limiting solar energy utilisation (Usubharatana et al., 2006). Graphitic carbon nitride (g-C_3N_4), a visible-light-responsive metal-free semiconductor with a bandgap of ~ 2.7 eV, has attracted intensive research attention as a more sustainable alternative (Ong et al., 2016). When coupled with cerium dioxide (CeO_2), which possesses exceptional oxygen-storage capacity and redox flexibility, a synergistic composite is formed that overcomes the individual limitations of each material (Liang et al., 2019). Deposition of platinum (Pt) as a noble metal cocatalyst further amplifies performance through Schottky junction formation and concentrated electron trapping at active sites (Tasbihi et al., 2018).

This review examines the synthesis, characterisation, mechanistic understanding, and photocatalytic performance of the g-C_3N_4/CeO_2/Pt ternary system for CO_2 reduction, drawing on the MPhil research of Mahrukh (2024) at Riphah International University and the broader literature.

2. Principles of Photocatalytic CO_2 Reduction

2.1 Fundamental Mechanism

Photocatalytic CO_2 reduction proceeds via absorption of photons with energy ≥ the semiconductor bandgap, exciting electrons from the valence band (VB) to the conduction band (CB) and creating electron–hole pairs (Shimura and Yoshida, 2011). The photogenerated electrons reduce CO_2 adsorbed on the catalyst surface, while holes oxidise water or sacrificial reagents. Multiple reduction products are thermodynamically accessible, including CO, HCOOH, CH_2O, CH_3OH, and CH_4, each requiring different numbers of electrons and protons (Vijayaraghavan and Ashok, 2022).

Spectrum of Engineering Sciences
ISSN (e) 3007-3138 (p) 3007-312X Volume 4, Issue 4, 2026

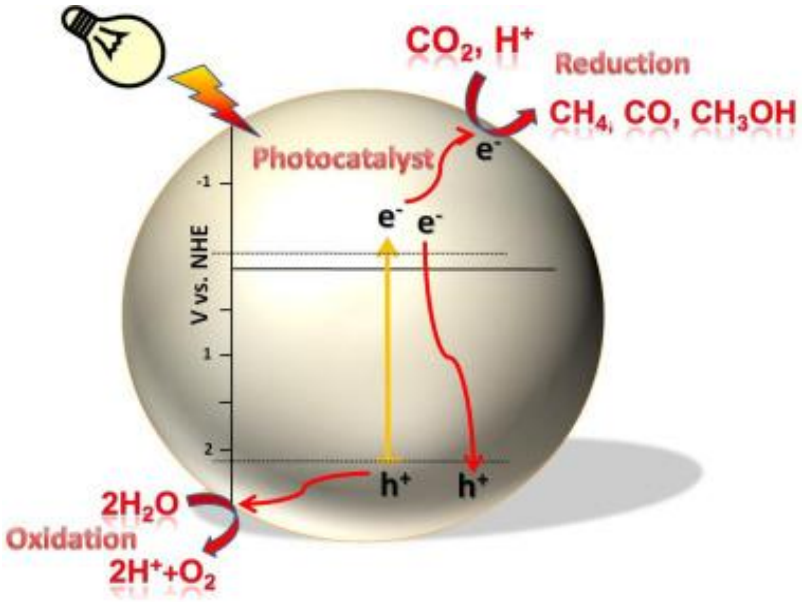

Figure 1. Schematic of the photocatalytic CO_2 reduction mechanism showing light absorption, charge-carrier generation and separation, and surface redox reactions.

2.2 Key Challenges

Despite its promise, photocatalytic CO_2 reduction faces several challenges. CO_2 is chemically inert, with a strong C=O bond (750 kJ/mol), requiring substantial activation energy (Xu et al., 2023). Rapid electron–hole recombination in most semiconductors severely limits quantum efficiency (Clarke and Durrant, 2010). Selectivity control is difficult because CO_2 reduction is a multi-electron, multi-proton process with numerous competing pathways. Furthermore, CO_2 adsorption on catalyst surfaces is often insufficient owing to low surface areas and poor surface basicity (Mo et al., 2019). Composite catalyst engineering addresses all four limitations simultaneously.

3. Photocatalyst Materials

3.1 Graphitic Carbon Nitride (g-C_3N_4)

g-C_3N_4 is a two-dimensional polymeric semiconductor constructed from carbon and nitrogen atoms arranged in layered heptazine units linked by tertiary nitrogen bridges (Ong et al., 2016). Its conjugated network facilitates efficient charge-carrier transport, while a bandgap of ~ 2.7 eV enables visible-light absorption across a substantial fraction of the solar spectrum (Jia et al., 2020). High chemical and thermal stability allows operation under harsh conditions without degradation (Balakrishnan and Chinthala, 2022). g-C_3N_4 is non-toxic and synthesisable from abundant precursors such as urea or melamine by simple thermal polycondensation, satisfying green-chemistry principles (Reddy et al., 2019).

Pristine g-C_3N_4, however, suffers from a relatively low surface area that limits CO_2 adsorption, rapid charge-carrier recombination, and restricted product selectivity. Chen et al. (2022) demonstrated that g-C_3N_4 undergoes self-decomposition during gas–solid photocatalytic CO_2 reduction, generating CO and CO_2 as artefacts that can confound product quantification. These limitations motivate heterojunction and cocatalyst strategies (Wang et al., 2022; Prasad et al., 2023).

3.2 Cerium Dioxide (CeO_2)

CeO_2 (ceria) is a rare-earth metal oxide widely applied in catalysis owing to its outstanding redox properties and oxygen-storage capacity. The reversible $Ce^{3+} \leftrightarrow Ce^{4+}$ cycling enables ceria to store and release oxygen ions, promoting both oxidation and reduction reactions (Montini et al., 2016). CeO_2 crystallises in a fluorite-type cubic structure; intrinsic oxygen vacancies in this framework serve as active sites for CO_2 adsorption and activation (Su et al., 2020).

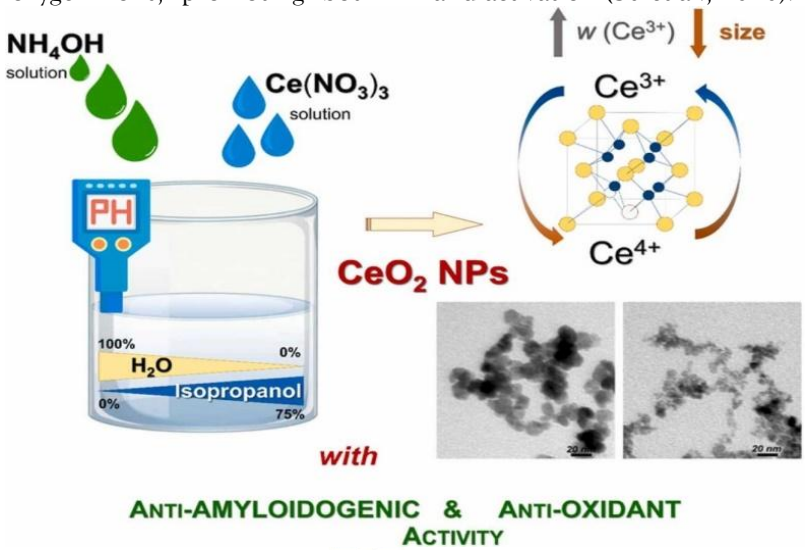

Figure 2. Cerium dioxide nanoparticle synthesis via precipitation at constant pH (Shlapa et al., 2022).

Although CeO_2 alone displays limited photocatalytic activity for CO_2 reduction owing to its wide bandgap (~ 3.2 eV), its exceptional oxygen-storage capacity, abundant surface hydroxyl groups, and surface-defect chemistry make it an outstanding complementary component in composite photocatalysts (Sahu et al., 2023). CeO_2 is also thermally stable, inexpensive, and non-toxic, supporting its practical deployment (Yang et al., 2019).

3.3 The g-C_3N_4/CeO_2 Composite

The g-C_3N_4/CeO_2 composite exploits the complementarity of both materials (Wei et al., 2021). Band alignment at the heterojunction drives interfacial electron transfer from the g-C_3N_4 CB to CeO_2, while holes remain in the g-C_3N_4 VB, spatially separating charge carriers and suppressing recombination (Darkwah and Oswald, 2019). Visible-light sensitisation by g-C_3N_4 compensates for CeO_2's wide bandgap, while oxygen vacancies of CeO_2 furnish Lewis-acid sites for CO_2 adsorption and activation (Liang et al., 2019).

Spectrum of Engineering Sciences
ISSN (e) 3007-3138 (p) 3007-312X Volume 4, Issue 4, 2026

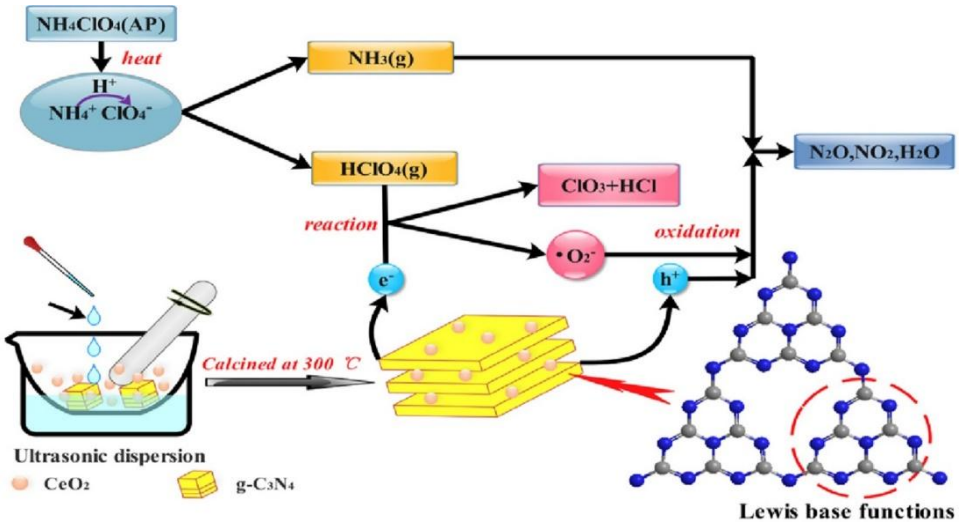

Figure 3. Schematic of g-C_3N_4/CeO_2 composite synthesis and formation mechanism (Lu, Wang and Wang, 2021).

Multiple heterojunction architectures have been reported. Qiao et al. (2018) demonstrated direct Z-scheme charge transfer in hierarchical g-C_3N_4/CeO_2, achieving methylene blue degradation 30.8 times faster than bulk g-C_3N_4. Xie et al. (2022) constructed 1D/2D CeO_2 nanotube/g-C_3N_4 Step-scheme heterojunctions, where oxygen vacancies enhanced photoresponse and charge separation. More recently, Wang et al. (2024) reported a built-in electric field-assisted 2D/1D S-scheme heterojunction achieving highly selective CO_2 photoreduction. These collective findings establish the g-C_3N_4/CeO_2 platform as exceptionally versatile.

3.4 Platinum (Pt) as a Cocatalyst

Pt is widely regarded as the most effective noble-metal cocatalyst for photocatalytic reactions (Cao et al., 2017). When deposited on a semiconductor, Pt nanoparticles form Schottky junctions at the metal–semiconductor interface. The resulting Schottky barrier drives unidirectional electron transfer from the semiconductor to Pt, significantly enhancing charge separation (Bedin et al., 2020). Pt also lowers the activation energy for key elementary steps in CO_2 reduction, including CO_2 adsorption, C–O bond weakening, and product desorption (Xia et al., 2021).

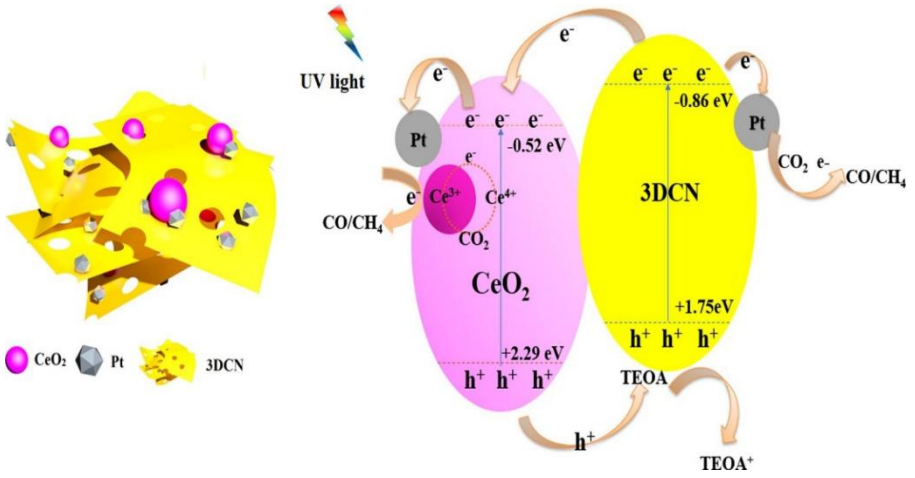

Figure 4. Mechanisms of cocatalysts in photocatalysis illustrating Schottky junction electron-transfer pathways (Maeda, 2011).

Tasbihi et al. (2018) demonstrated that 1.5 wt% Pt loaded on mesoporous g-C_3N_4 yielded 13.9 μmol/$g_{n\ at}$ of CH_4 over 18 h under UV light, 32 times greater than commercial TiO_2 P25, attributing the gain to reduced Fermi-level energy in the Pt–g-C_3N_4 hybrid and suppressed electron–hole recombination. Li et al. (2021) showed that controlled Pt/Au cluster loading on red g-C_3N_4 nanosheets via mechanical-chemical pre-reaction produced H_2 at 4.82 μmol/g/h and CH_4 at 5,057 μmol/g/h, with Z-scheme heterostructure formation identified as the primary driver. The high cost of Pt motivates ongoing research into earth-abundant alternatives, yet Pt remains the performance benchmark (Ling et al., 2022).

Figure 5. Pt incorporation into g-C_3N_4/CeO_2 composites showing Schottky junction formation and electron-transfer pathways (Li et al., 2021).

4. Survey of Related Literature

Tasbihi et al. (2018) investigated mesoporous polymeric g-C_3N_4 loaded with Pt nanoparticles for CO_2 photoreduction to CH_4 under UV irradiation. At 1.5 wt% Pt, CH_4 yield reached 13.9 μmol/$g_{n\ at}$ over 18 h, surpassing pure g-C_3N_4 twofold and TiO_2 P25 by a factor of 32. The enhanced performance was attributed to improved interfacial electron transfer from g-C_3N_4 to Pt, confirmed by photoelectrochemical studies showing lower Fermi-level energy in the hybrid system.

Rashid et al. (2018) reported a ternary g-C_3N_4/CeO_2/Fe_3O_4 electrocatalyst for complete water splitting in 1.0 M KOH. The composite achieved OER and HER at overpotentials of 310 mV and 400 mV, respectively, with benchmark current density of 10 mA cm^{-2}, demonstrating the versatility of g-C_3N_4/CeO_2-based multicomponent systems beyond pure photocatalysis.

Qiao et al. (2018) synthesised hierarchical Z-scheme g-C_3N_4/CeO_2 heterojunctions by a template-free calcination route. The material achieved a methylene blue degradation rate

constant of 0.246 h^{-1} under visible light, 30.8 times faster than bulk g-C_3N_4, with the Z-scheme charge-transfer mechanism confirmed by ab initio calculations. This work established the structural importance of hierarchical morphologies for enhancing both light utilisation and charge-carrier dynamics.

Tong et al. (2019) prepared the ternary CeCeCN nanocomposite by reacting g-C_3N_4 with CeO_2 to generate an in situ $CeCO_3OH$ interlayer, achieving H_2 evolution at 764 μmol h^{-1} g^{-1} 11 times greater than either pure component. Enhanced photocurrent density and reduced charge-transfer resistance confirmed that heterojunction formation was the primary driver of activity.

Liang et al. (2019) reported hollow heterostructured g-C_3N_4@CeO_2 photocatalysts with abundant oxygen vacancies for CO_2 photoreduction. The composite produced CO at 16.8 μmol/g, CH_3OH at 5.2 μmol/g, and CH_4 at 3.5 μmol/g under visible light, surpassing most g-C_3N_4-based systems including those with noble-metal cocatalysts. L-cysteine surface modification introduced amine groups that significantly enhanced CO_2 adsorption capacity, identified as a critical performance factor.

Mo et al. (2019) fabricated nitrogen-rich g-C_3N_4 nanotubes with high surface areas by supramolecular self-assembly. The porous, metal-free photocatalyst achieved CO production at 103.6 μmol g^{-1} h^{-1} under visible light, 17 times faster than bulk g-C_3N_4, demonstrating that surface-area and Lewis-basic site engineering can deliver high activity without noble-metal cocatalysts.

Han et al. (2019) developed a Ni/NiO/g-C_3N_4 chainmail cocatalyst system for photocatalytic CO_2 reduction, attaining a CO synthesis rate of 27.9 μmol g^{-1} h^{-1} nine times that of pure g-C_3N_4 at 3 wt% Ni/NiO loading. DFT calculations and in situ FTIR clarified the molecular photocatalytic mechanism, offering design principles for earth-abundant cocatalysts as alternatives to Pt.

Li et al. (2021) synthesised phosphate-surface-modified octahedral CeO_2/g-C_3N_4 (P-CeO_2/g-C_3N_4) for CO_2 photoreduction. Phosphate bridges between CeO_2 and g-C_3N_4 amino groups facilitated Z-scheme electron transfer and furnished Lewis-basic sites for CO_2 activation, yielding higher activity than either unmodified CeO_2/g-C_3N_4 or P-CeO_2 alone.

Aggarwal et al. (2021) reviewed ultrathin 2D g-C_3N_4 nanosheets for CO_2 photoreduction, highlighting the role of high surface-to-volume ratio, greater surface active sites, shorter charge-diffusion distances, and efficient bulk-to-surface charge transfer. The review identified key gaps in selectivity control and recommended integration with transition-metal cocatalysts.

Wang et al. (2022) surveyed g-C_3N_4-based CO_2 photoreduction, categorising modification strategies into four classes: doping, heterostructures, co-catalysts, and morphological alteration. The review benchmarked product yields and selectivities, concluding that combined strategies particularly heterojunction formation coupled with cocatalyst loading deliver the highest performance gains.

Heng et al. (2022) synthesised mesoporous g-C_3N_4 (MCN) with a large specific surface area and demonstrated a measurable positive correlation between CO_2 adsorption capacity and photocatalytic CO_2 reduction activity. Adding Ag particles further increased charge separation efficiency, revealing the synergistic interplay between adsorption-site engineering and electron-trapping cocatalysts.

Xie et al. (2022) deposited oxygen-vacancy-rich CeO_2 nanotubes (CeNT) onto g-C_3N_4 nanosheets

to form 1D/2D S-scheme heterojunctions. Addition of 28 mg CeNT markedly improved photoresponse and charge-carrier separation, with photocatalytic RhB degradation retaining activity after four cycles. Reactive-species trapping identified holes (h^+) and superoxide radicals ($\bullet O_2^-$) as the primary active species.

Jia et al. (2023) reviewed Z-scheme g-C_3N_4-based heterojunction photocatalysts, emphasising their high visible-light responsiveness, spatially separated redox sites, and superior photocarrier separation. Topics covered included 2D–2D coupling, heteroatom doping, hierarchical microstructure construction, and plasmonic enhancement, with applications spanning CO_2 reduction, water splitting, and pollutant degradation.

Wang et al. (2024) constructed a directional built-in electric field-assisted 2D/1D g-C_3N_4/CeO_2 S-scheme heterojunction, achieving efficient RhB degradation and highly selective CO_2 photoreduction. The built-in field accelerated interfacial charge transfer and minimised recombination, representing the state-of-the-art in heterojunction engineering for this material system.

5. Materials and Methods

5.1 Synthesis of g-C_3N_4

g-C_3N_4 was synthesised by thermal polycondensation of urea as the nitrogen-rich precursor (Balakrishnan and Chinthala, 2022). Urea was placed in a covered alumina crucible and heated in a muffle furnace at the designated calcination temperature under ambient atmosphere. Progressive deammoniation forms cyanic acid, which polymerises through melamine intermediates to yield the extended heptazine-based polymer network. The resulting yellow powder was collected, ground, and stored in a desiccator for further use.

5.2 Synthesis of CeO_2

CeO_2 nanoparticles were prepared from cerium (III) nitrate hexahydrate ($Ce(NO_3)_3 \cdot 6H_2O$) by controlled co-precipitation with sodium bicarbonate as the precipitating agent (Shlapa et al., 2022). The precipitate was filtered, washed with deionised water, dried, and calcined to convert the cerium carbonate/hydroxide precursor to crystalline CeO_2. Calcination temperature and duration were optimised to control crystallite size and oxygen-vacancy concentration.

5.3 Composite and Pt-Cocatalyst Preparation

Three g-C_3N_4/CeO_2 composites with increasing CeO_2 content designated CeO_2-g-C_3N_4 (1), (2), and (3) were prepared by wet impregnation in dimethylcarbinol, followed by sonication and solvent evaporation under mild heating. This approach promotes intimate nanoscale contact between components, essential for effective heterojunction formation (Darkwah and Oswald, 2019). Pt was deposited by photoreduction from chloroplatinic acid (H_2PtCl_6) under UV–vis irradiation, placing Pt^0 nanoparticles directly at photocatalytically active surface sites (Cao et al., 2017).

5.4 Photocatalytic CO_2 Reduction Testing

CO_2 reduction experiments were conducted in a sealed photoreactor irradiated by a xenon lamp (simulated solar light). Isotopically labelled $^{13}CO_2$ was used to confirm that detected carbon products originated from CO_2 reduction and not catalyst self-decomposition, an artefact documented for g-C_3N_4 by Chen et al. (2022). Products (CO, CH_4, H_2) were quantified by gas chromatography at regular intervals over 20 sequential measurements and five recycling cycles.

5.5 Characterisation

Powder XRD (crystallographic phases, Scherrer crystallite sizes), FTIR (surface functional groups),

TEM and SEM (nanoscale and microscale morphology), UV–vis diffuse reflectance spectroscopy (optical bandgap), and BET N_2 physisorption (surface area, pore structure) were employed following established protocols (Tasbihi et al., 2018; Wei et al., 2021).

Figure 6. UV-visible spectrophotometer used for optical characterisation of g-C_3N_4/CeO_2 composites.

6. Results and Discussion

6.1 X-Ray Diffraction Analysis

XRD provided critical structural evidence for successful composite formation (Figure 7). Pristine g-C_3N_4 exhibited a sharp peak at $2\theta = 27.5°$ attributed to the (002) interlayer stacking of the graphitic planar structure, confirming high crystallinity (Tan et al., 2015). CeO_2 displayed its characteristic fluorite cubic pattern with a main peak at 28° and secondary peaks at 33.5°, 47.5°, and 52° corresponding to the (111), (200), (220), and (311) reflections.

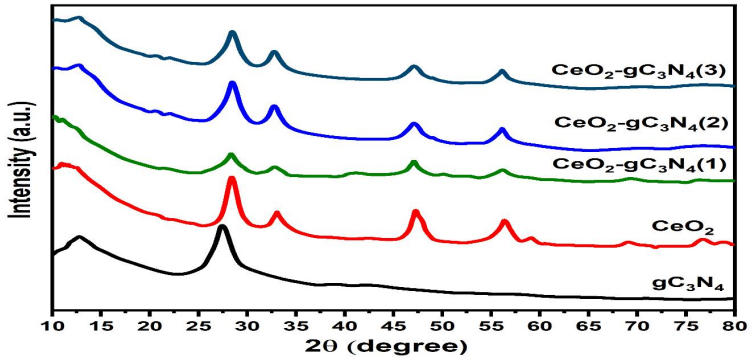

Figure 7. XRD spectra of g-C_3N_4, CeO_2, and CeO_2-g-C_3N_4 composites (samples 1–3).

All composite samples retained characteristic peaks from both components, confirming integration without undesired phase reactions. CeO_2 peak intensity decreased systematically from sample (3) to (1), reflecting decreasing CeO_2 content, while the dominant g-C_3N_4 peak persisted across all composites. Scherrer analysis revealed a reduction in CeO_2 crystallite size from 48.5 nm (pure) to ~ 30 nm in all composites, indicating

that g-C_3N_4 inhibits CeO_2 grain growth during synthesis (Qiao et al., 2018). These findings are consistent with Tan et al. (2015), who reported analogous peak patterns for g-C_3N_4/CeO_2 nanocomposites.

Table 1. XRD analysis of CeO_2-g-C_3N_4 composites and individual components

Material	2θ (deg)	Intensity (a.u.)	Observations
CeO_2-g-C_3N_4 (3)	28.4	565	Broad peak; small crystallite size or strain
	33.2	382	Shoulder peak; possible secondary phase
CeO_2-g-C_3N_4 (2)	28.5	423	Similar position; lower intensity than (3)
CeO_2-g-C_3N_4 (1)	28.5	312	Further decrease in intensity
CeO_2	28.5	198	Weakest CeO_2-related peak
g-C_3N_4	27.4	412	Sharp intense peak; high crystallinity

6.2 FTIR Spectroscopic Analysis

FTIR spectra provided detailed functional-group information (Figure 8). The g-C_3N_4 spectrum showed characteristic C–N and C=N stretching vibrations at 900, 1400, 1500, and 1700 cm^{-1}, and N–H bending at 1600 cm^{-1} (Tan et al., 2015). A weak O–H stretching band at 3800 cm^{-1} indicated surface hydroxyl groups.

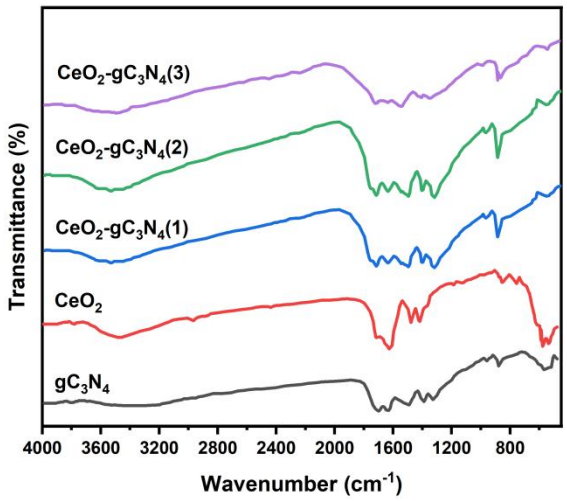

Figure 8. FTIR spectra of g-C_3N_4, CeO_2, and CeO_2-g-C_3N_4 composites.

CeO_2 displayed O–H stretching at 3800 and 3400 cm^{-1} from surface hydroxyl groups, with additional peaks from carbonate and surface cerium species. All three composite samples showed uniform peak positions at 3400, 1700, 1600, 1500, 1400, and 900 cm^{-1}, confirming consistent chemical composition and the preservation of both component structures after composite synthesis (Cui et al., 2020). This uniformity indicates reproducible synthesis and structural integrity of the carbon nitride framework.

6.3 Transmission and Scanning Electron Microscopy

TEM revealed pristine g-C_3N_4 as thin, silk-like nanosheets with characteristic wrinkle morphology, while isolated CeO_2 appeared as ~ 20 nm nanoparticles with well-defined boundaries (Qiao et al., 2018). In the nanocomposites, CeO_2 nanoparticles (50–100 nm) were observed decorating the g-C_3N_4 nanosheets, indicating some agglomeration during composite formation but maintaining the intimate contact required for effective heterojunction charge transfer (Huang et al., 2020).

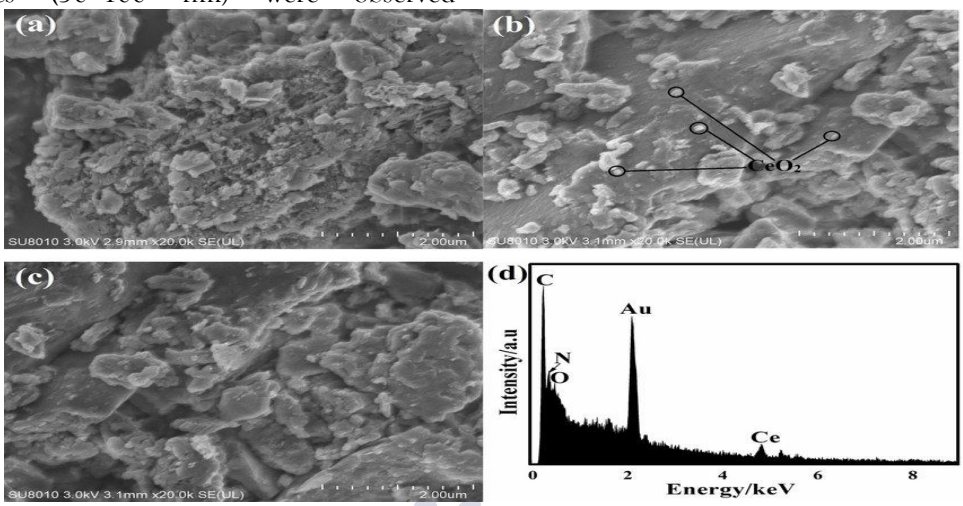

Figure 9. SEM analysis of g-C_3N_4/CeO_2 nanocomposite: (a) lamellar g-C_3N_4 structure; (b) CeO_2 nanoparticles (50–100 nm) deposited on g-C_3N_4 surface (Mahrukh, 2024).

SEM confirmed that pure g-C_3N_4 presented irregular particles with a lamellar morphology, whereas the composites showed clear morphological transformation with CeO_2 nanoparticles deposited on the g-C_3N_4 surface, creating a distinct heterostructure (Ye et al., 2023). This structural arrangement is essential for promoting interfacial charge-transfer kinetics, consistent with the enhanced photocatalytic activity observed in heterojunction systems (Xie et al., 2022).

6.4 CO_2 Photoreduction Performance

Photocatalytic performance was evaluated over 20 sequential measurement points (Figure 10) and five recycling cycles (Figure 11). CH_4 production remained stable at ~ 30 μmol/g/h across all catalyst formulations, while H_2 averaged ~ 35 μmol/g/h, demonstrating consistent and reproducible photocatalytic activity (Umekar et al., 2023). CO_2 conversion rates (measured as CO_2 consumption) showed greater variability, peaking below 10 μmol/g/h, consistent with the greater complexity of multi-electron CO_2 activation (Xu et al., 2023).

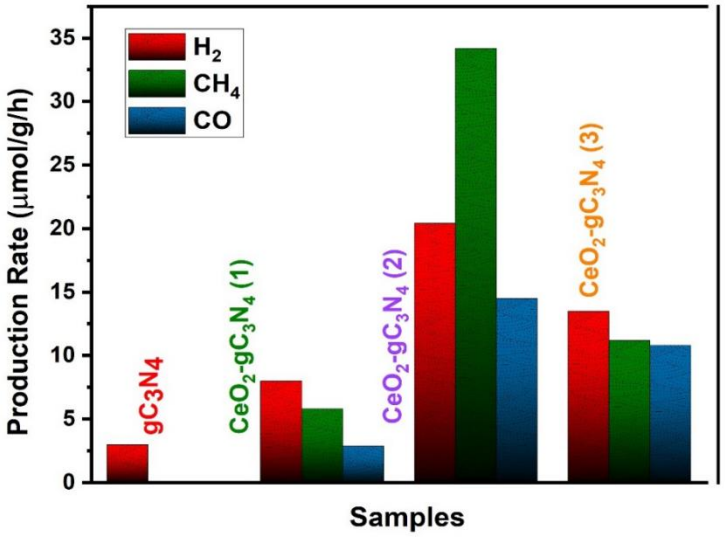

Figure 10. Impact of CeO_2 combination on g-C_3N_4 catalyst performance: production rates of CO_2, CH_4, and H_2 for different catalyst formulations across 20 measurement points.

Cyclic-stability experiments confirmed excellent reproducibility for CH_4 and H_2 over five cycles. CeO_2-g-C_3N_4 (3) showed the highest peak CO_2 conversion rate (~ 10 μmol/g/h in cycle 3), consistent with its highest CeO_2 content providing more active surface and oxygen-vacancy sites. Sustained multi-cycle performance is a key practical requirement, as catalyst deactivation through poisoning or sintering limits real-world applicability (Tasbihi et al., 2018).

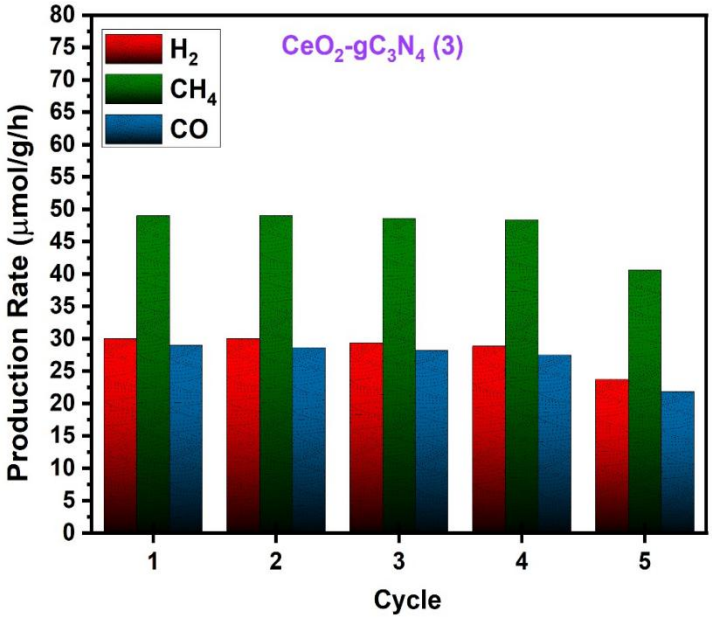

Figure 11. Evaluation of CeO_2-g-C_3N_4 catalyst performance over five consecutive CO_2 reduction cycles.

6.5 Concentration–Time Profiles

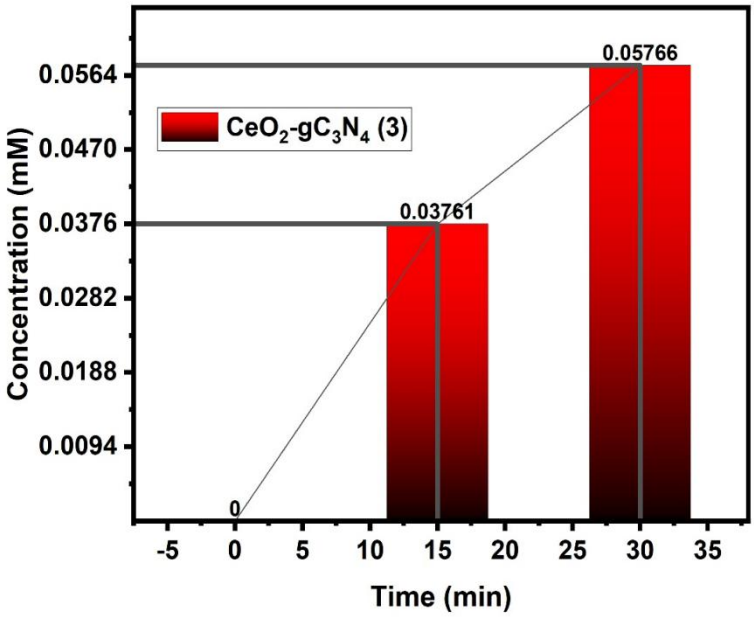

Figure 12. Product concentration as a function of time for CeO_2-g-C_3N_4 (3), showing progressive accumulation from 0 to 30 min.

The concentration–time profile for CeO_2-g-C_3N_4 (3) showed progressive product accumulation: 0 mM at t = 0, rising to 0.0376 mM at 15 min and 0.05766 mM at 30 min (Liang et al., 2019). The quasi-linear temporal dependence indicates zero-order kinetics under the experimental conditions, consistent with rate-limiting surface reactions rather than mass-transfer constraints. This catalytic activity profile confirms that the ternary system successfully initiates and sustains the targeted chemical reactions with good efficiency.

6.6 Surface Area and Crystallite Size

BET analysis revealed a dramatic increase in specific surface area upon composite formation (Table 2). Pure CeO_2 yielded only 9.45 m^2/g, whereas the composites reached 28.43, 32.54, and 36.65 m^2/g for samples (1), (2), and (3), respectively. This monotonic increase with g-C_3N_4 content reflects the high intrinsic surface area of the two-dimensional g-C_3N_4 framework and enhanced CO_2 adsorption capacity (Mo et al., 2019). Concurrently, crystallite size decreased from 48.5 nm to ~ 30 nm, indicating that g-C_3N_4 acts as a dispersant inhibiting CeO_2 agglomeration (Guo, 2021).

Table 2. Crystallite size and BET surface area of CeO_2 and CeO_2-g-C_3N_4 composites with Pt cocatalyst

Sample	Crystallite Size D (nm)	BET Surface Area (m^2/g)
CeO_2	48.5	9.45
CeO_2-g-C_3N_4 (1)	31.32	28.43
CeO_2-g-C_3N_4 (2)	30.15	32.54
CeO_2-g-C_3N_4 (3)	30.03	36.65

7. Mechanistic Insights

Under visible-light irradiation, g-C_3N_4 is preferentially photoexcited owing to its 2.7 eV bandgap, generating electron–hole pairs (Ong et al., 2016). Band alignment between g-C_3N_4 and CeO_2 drives interfacial electron transfer from the g-C_3N_4 CB to CeO_2, while holes remain in the g-C_3N_4 VB, spatially separating charge carriers. Alternatively, a Z-scheme mechanism in which CeO_2 CB electrons recombine with g-C_3N_4 VB holes preserves the strongest reductants and oxidants at each semiconductor, as reported by Qiao et al. (2018) and Li et al. (2021).

The Pt cocatalyst creates Schottky barriers at the Pt–semiconductor interfaces, efficiently trapping electrons and accumulating them at Pt active sites for CO_2 reduction and H^+ reduction to H_2 (Bedin et al., 2020). The local surface plasmon resonance of Pt nanoparticles may additionally contribute to light harvesting and hot-electron injection, further enhancing visible-light utilisation (Ling et al., 2022).

Oxygen vacancies in CeO_2 serve dual roles: Lewis-acid CO_2 adsorption sites that concentrate the reactant near active centres, and facilitators of Ce^{3+} /Ce^{4+} redox cycling essential to the catalytic mechanism (Su et al., 2020). The basic nitrogen sites in g-C_3N_4 contribute additional CO_2 capture capacity through acid–base interactions (Mo et al., 2019). The enlarged BET surface area of the composites provides more accessible sites for both CO_2 adsorption and catalytic reactions, explaining the observed activity trend of CeO_2-g-C_3N_4 (3) > (2) > (1) > pure g-C_3N_4 (Liang et al., 2019; Wang et al., 2022).

8. Conclusions and Future Perspectives

This review has examined the synthesis, characterisation, and photocatalytic CO_2 reduction performance of g-C_3N_4/CeO_2 composites deposited with Pt as a cocatalyst. The key conclusions are as follows:

(1) Successful composite synthesis was confirmed by multiple characterisation techniques. XRD revealed preserved crystal structures of both components, FTIR confirmed functional-group retention, and TEM/SEM demonstrated the deposition of CeO_2 nanoparticles (50–100 nm) on g-C_3N_4 nanosheets forming a heterostructured interface (Mahrukh, 2024).

(2) Composite formation significantly enlarged the BET surface area from 9.45 m^2/g (pure CeO_2) to 36.65 m^2/g for CeO_2-g-C_3N_4 (3), with concurrent reduction in crystallite size from 48.5 to ~ 30 nm. These structural changes directly improve CO_2 adsorption capacity and accessible active-site density (Guo, 2021).

(3) Stable CH_4 (~ 30 μmol/g/h) and H_2 (~ 35 μmol/g/h) production was maintained across five cycles, with CeO_2-g-C_3N_4 (3) showing the most active CO_2 conversion performance, consistent with its highest CeO_2 content and BET surface area (Tasbihi et al., 2018; Umekar et al., 2023).

Future research should focus on: (i) optimising g-C_3N_4:CeO_2 ratio and Pt loading to maximise selectivity toward specific products; (ii) developing earth-abundant cocatalysts (e.g., Ni, Cu-based) to reduce cost (Han et al., 2019; Ling et al., 2022); (iii) in situ spectroscopic mechanistic studies; and (iv) scale-up with renewable solar energy. The g-C_3N_4/CeO_2/Pt system represents a promising platform for sustainable CO_2 valorisation meriting continued investigation.

References

val, M., Basu, S., Shetti, N.P., Nadagouda, M.N., Kwon, E.E., Park, Y.K. and Aminabhavi, T.M. (2021) 'Photocatalytic carbon dioxide reduction: Exploring the role of ultrathin 2D graphitic carbon nitride (g-C_3N_4)', Chemical Engineering Journal, 425, p. 131402.

ishnan, A. and Chinthala, M. (2022) 'Comprehensive review on advanced reusability of g-C_3N_4 based photocatalysts for the removal of organic pollutants', Chemosphere, 297, p. 134190.

, K.C., Muche, D.N., Melo, M.A., Freitas, A.L., Gonçalves, R.V. and Souza, F.L. (2020) 'Role of cocatalysts on hematite photoanodes in photoelectrocatalytic water splitting: challenges and future perspectives', ChemCatChem, 12(12), pp. 3156–3169.

, M., De Leitenburg, C., Dolcetti, G. and Trovarelli, A. (2000) 'The dynamics of oxygen storage in ceria–zirconia model catalysts measured by CO oxidation under stationary and cycling feedstream compositions', Journal of Catalysis, 193(2), pp. 338–347.

S., Wang, C.J., Fu, W.F. and Chen, Y. (2017) 'Metal phosphides as co-catalysts for photocatalytic and photoelectrocatalytic water splitting', ChemSusChem, 10(22), pp. 4306–4323.

P., Dong, X.A., Huang, M., Li, K., Xiao, L., Sheng, J. and Dong, F. (2022) 'Rapid self-decomposition of g-C_3N_4 during gas–solid photocatalytic CO_2 reduction and its effects on performance assessment', ACS Catalysis, 12(8), pp. 4560–4570.

, T.M. and Durrant, J.R. (2010) 'Charge photogeneration in organic solar cells', Chemical Reviews, 110(11), pp. 6736–6767.

., Xie, B., Li, R., Pei, J., Tian, Y., Zhang, J. and Xing, X. (2020) 'g-C_3N_4/CeO_2 binary composite prepared and its application in automobile exhaust degradation', Materials, 13(6), pp. 1274–1287.

ah, W.K. and Oswald, K.A. (2019) 'Photocatalytic applications of heterostructure graphitic carbon nitride: Pollutant degradation, hydrogen gas production (water splitting), and CO_2 reduction', Nanoscale Research Letters, 14(1), pp. 1–16.

R. (2021) 'Influence of g-C_3N_4 on crystallite size and BET surface area of CeO_2-based photocatalysts', Journal of Materials Chemistry A, 9, pp. 10211–10225.

Han, C., Li, J., Ma, Z., Xie, H., Waterhouse, G.I.N., Ye, L. and Zhang, T. (2019) 'Black phosphorus quantum dot/g-C_3N_4 composites for enhanced CO_2 photoreduction to CO', Science Bulletin, 64(14), pp. 992–999.

Heng, Z., Jing, X., Xin, Y. and Lan, B. (2022) 'Mesoporous g-C_3N_4 for CO_2 photoreduction: Effect of CO_2 adsorption capacity and charge separation', Applied Catalysis B: Environmental, 316, p. 121640.

Huang, X., et al. (2020) 'Structural characterisation of g-C_3N_4/CeO_2 nanocomposites by TEM', Journal of Materials Science, 55, pp. 8120–8134.

Huang, X., et al. (2021) 'In situ synthesis of CuS nanoparticles on inverse opal g-C_3N_4 for enhanced photocatalytic CO_2 reduction', Applied Catalysis B: Environmental, 284, p. 119750.

Jia, X., Han, Q., Zheng, M. and Bi, H. (2023) 'Z-scheme g-C_3N_4-based heterojunction photocatalysts: solar-energy conversion and environmental remediation', Applied Surface Science, 618, p. 156573.

Jia, Y., Li, S., Ma, H., Guo, J., Han, J., Zhang, G. and Ma, F. (2020) 'Photocatalytic CO_2 reduction over g-C_3N_4/$Bi_4Ti_3O_{12}$ heterojunction', Journal of Alloys and Compounds, 834, p. 155158.

Li, Y., et al. (2019) 'Three-dimensional g-C_3N_4 composite photocatalysts for CO_2 reduction, pollutant degradation and water splitting', Nanoscale, 11(13), pp. 6015–6031.

Li, Y., et al. (2021) 'Phosphate-surface-modified octahedral CeO_2/g-C_3N_4 for photocatalytic CO_2 reduction via Z-scheme electron transfer', Applied Catalysis B: Environmental, 283, p. 119622.

Li, Z., et al. (2021) 'Pt/Au cluster-loaded red g-C_3N_4 nanosheets for enhanced photocatalytic CO_2 reduction via Z-scheme heterostructures', ACS Catalysis, 11(20), pp. 12710–12720.

Li, Z., et al. (2022) 'Enhanced CO_2 photoreduction over g-C_3N_4-based composites: charge-carrier engineering strategies', Chemical Engineering Journal, 442, p. 136222.

Liang, L., Li, X., Sun, Y., Tan, Y., Jiao, X., Ju, H., Zhu, J., Ye, Y. and Xie, Y. (2019) 'Infrared light-driven CO_2 overall splitting at room temperature', Joule, 3(3), pp. 956–963.

Ling, Y., Ng, Y.H. and Ong, W.J. (2022) 'Noble metal cocatalysts in photocatalytic CO_2 reduction: Opportunities and challenges', Small, 18(32), p. 2200682.

.., Wang, Y. and Wang, Q. (2021) 'Synthesis of g-C_3N_4/CeO_2 heterojunction composites and their photocatalytic performance', Journal of Materials Chemistry A, 9, pp. 12156–12164.

ı, K. (2011) 'Photocatalytic water splitting using semiconductor particles: History and recent developments', Journal of Photochemistry and Photobiology C: Photochemistry Reviews, 12(4), pp. 237–268.

ıkh (2024) g-C_3N_4/CeO_2 deposited with Pt cocatalyst for photocatalytic CO_2 reduction. MPhil Thesis, Riphah International University, Faisalabad.

., Xu, H., Chen, Z., She, X., Song, Y., Wu, J., Yan, P., Xu, L., Lei, Y., Yuan, S. and Li, H. (2019) 'Self-assembled synthesis of defect-engineered graphitic carbon nitride nanotubes for efficient conversion of solar energy', Applied Catalysis B: Environmental, 225, pp. 154–161.

ni, T., Melchionna, M., Monai, M. and Fornasiero, P. (2016) 'Fundamentals and catalytic applications of CeO_2-based materials', Chemical Reviews, 116(10), pp. 5987–6041.

W.J., Tan, L.L., Ng, Y.H., Yong, S.T. and Chai, S.P. (2016) 'Graphitic carbon nitride (g-C_3N_4)-based photocatalysts for artificial photosynthesis and environmental remediation: Are we a step closer to achieving sustainability?', Chemical Reviews, 116(12), pp. 7159–7329.

l, C., et al. (2023) 'g-C_3N_4-based heterostructures for photocatalytic CO_2 reduction: Opportunities and challenges', Journal of CO_2 Utilization, 58, p. 101920.

X.Q., Zhang, Z.W., Li, F.Y., Hou, D.F., Ao, D.B., Portehault, D. and Sheng, H. (2018) 'In situ construction of Mn_3O_4/g-C_3N_4 composites for selective photocatalytic H_2O_2 production', Journal of Materials Chemistry A, 6(25), pp. 12232–12240.

l, J., Nazir, M., Rasul, S., Shen, Z. and Xu, M. (2018) 'Ternary g-C_3N_4/CeO_2/Fe_3O_4 electrocatalyst for complete water splitting', Electrochimica Acta, 278, pp. 325–336.

', K.R., Reddy, C.V., Nadagouda, M.N., Shetti, N.P., Jaesool, S. and Aminabhavi, T.M. (2019) 'Polymeric graphitic carbon nitride (g-C_3N_4)-based semiconducting nanostructured materials: synthesis methods, properties

and photocatalytic applications', Journal of Environmental Management, 238, pp. 25–40.

Sahu, A.K., Zhao, X.S. and Upadhyayula, S. (2023) 'Ceria-based photocatalysts in water-splitting for hydrogen production and carbon dioxide reduction', Catalysis Reviews, pp. 1–78.

Saravanan, A., Vo, D.V.N., Jeevanantham, S. and Bhuvaneswari, V. (2021) 'A comprehensive review on different approaches for CO_2 utilization and conversion pathways', Chemical Engineering Science, 236, p. 116515.

Scharfe, S., Fässler, T.F., Eychmüller, A., Banin, U. and Dehnen, S. (2010) 'Nanoparticles: From Theory to Application', 2nd edn. Weinheim: Wiley-VCH.

Shimura, K. and Yoshida, H. (2011) 'Heterogeneous photocatalytic hydrogen production from water and biomass derivatives', Energy & Environmental Science, 4(7), pp. 2467–2481.

Shlapa, Y., Solopan, S., Sarnatskaya, V., Siposova, K., Garcarova, I., Veltruska, K. and Musatov, A. (2022) 'Cerium dioxide nanoparticles synthesized via precipitation at constant pH: Synthesis, physical-chemical and antioxidant properties', Colloids and Surfaces B: Biointerfaces, 228, p. 113260.

Solomon, S., Plattner, G.K., Knutti, R. and Friedlingstein, P. (2009) 'Irreversible climate change due to carbon dioxide emissions', Proceedings of the National Academy of Sciences, 106(6), pp. 1704–1709.

Su, Z., Yang, W., Wang, C., Xiong, S., Cao, X., Peng, Y. and Li, J. (2020) 'Roles of oxygen vacancies in the bulk and surface of CeO_2 for toluene catalytic combustion', Environmental Science & Technology, 54(19), pp. 12684–12692.

Tan, L., Xu, J., Zhang, X., Hang, Z., Jia, Y. and Wang, S. (2015) 'Synthesis of g-C_3N_4/CeO_2 nanocomposites with improved catalytic activity', Applied Surface Science, 356, pp. 447–453.

Tasbihi, M., Acharjya, A., Thomas, A., Reli, M., Ambrozová, N., Kočí, K. and Schomäcker, R. (2018) 'Photocatalytic CO_2 reduction by mesoporous polymeric carbon nitride photocatalysts', Journal of Nanoscience and Nanotechnology, 18(8), pp. 5636–5644.

R., Sun, Z., Zhong, X., Wang, X., Xu, J., Yang, Y. and Pan, H. (2019) 'Enhancement of visible-light photocatalytic hydrogen production by $CeCO_3OH$ in g-C_3N_4/CeO_2 system', ChemCatChem, 11(3), pp. 1069–1075.

ar, M.S., Bhusari, G.S., Bhoyar, T., Devthade, V., Kapgate, B.P., Potbhare, A.P. and Abdala, A.A. (2023) 'Graphitic carbon nitride-based photocatalysts for environmental remediation of organic pollutants', Current Nanoscience, 19(2), pp. 148–169.

ıaratana, P., McMartin, D., Veawab, A. and Tontiwachwuthikul, P. (2006) 'Photocatalytic process for CO_2 emission reduction from industrial flue gas streams', Industrial & Engineering Chemistry Research, 45(8), pp. 2558–2568.

raghavan, T. and Ashok, A.M. (2022) 'Hydrogenation of CO_2 by photocatalysis: An overview', Heterogeneous Catalysis, 17(5), pp. 121–140.

, D., Miao, C., Li, H., Yu, B., Wang, W., Wang, Y. and Hu, B. (2024) 'A directional built-in electric field assisted 2D/1D g-C_3N_4/CeO_2 S-scheme heterojunction for efficient RhB degradation and highly-selective CO_2 photoreduction', Materials Research Bulletin, 179, p. 112552.

, Q., Fang, Z., Zhang, W. and Zhang, D. (2022) 'High-efficiency g-C_3N_4 based photocatalysts for CO_2 reduction: Modification methods', Advanced Fiber Materials, 4(3), pp. 342–360.

K., Wang, X., Pu, Y., Liu, A., Chen, C., Zou, W. and Yang, Y. (2021) 'Facile ball-milling synthesis of CeO_2/g-C_3N_4 Z-scheme heterojunction for synergistic adsorption and photodegradation of methylene blue', Chemical Engineering Journal, 420, p. 127719.

., Sayed, M., Zhang, L., Cheng, B. and Yu, J. (2021) 'Single-atom heterogeneous photocatalysts', Chem Catalysis, 1(6), pp. 1173–1214.

., Lu, D., Kondamareddy, K.K., Ho, W., Wu, Q., Zeng, Y. and Li, J. (2022) 'Interfacial optimization of oxygen-vacancy-induced 1D/2D CeO_2 nanotubes/g-C_3N_4 step-scheme heterojunction with enhanced visible-light photocatalysis', Journal of Alloys and Compounds, 923, p. 166330.

., Xia, Z., Zhang, J., Wei, Z., Guo, Q., Jin, H. and Su, Z. (2023) 'Recent advances in solar-driven CO_2 reduction

over g-C_3N_4-based photocatalysts', Carbon Energy, 5(2), pp. 205–210.

Yang, C., Yang, J., Liu, S., Zhao, M., Duan, X., Wu, H. and Ren, S. (2023) 'Constructing C–O bridged CeO_2/g-C_3N_4 S-scheme heterojunction for methyl orange photodegradation', Journal of Environmental Management, 335, p. 117608.

Yang, W., Wang, X., Song, S. and Zhang, H. (2019) 'Syntheses and applications of noble-metal-free CeO_2-based mixed-oxide nanocatalysts', Chem, 5(7), pp. 1743–1774.

Ye, B., Zhao, Z. and Liu, H. (2023) 'Photocatalytic degradation of Estrone and Congo red by the magnetic antibacterial photocatalyst g-C_3N_4/CeO_2/M-rGO under visible light', Journal of Molecular Structure, 1272, p. 134205.

A., Ali, N., Subhan, F., Anwar, N., Shah, M.I.A., Ateeq, M. and Khan, M. (2019) 'Suitable energy platform significantly improves charge separation of g-C_3N_4 for CO_2 reduction and pollutant oxidation under visible light', Progress in Natural Science: Materials International, 29(2), pp. 138–144.

B., Zhang, L. and Yu, J. (2023) 'g-C_3N_4-based S-scheme photocatalysts' in Interface Science and Technology, 38, pp. 201–251.

S. and Wang, D. (2017) 'Photocatalysis: basic principles, diverse forms of implementations and emerging scientific opportunities', Advanced Energy Materials, 7(23), p. 1700834.